

Article

A Physically Based Model for the Streaming Potential Coupling Coefficient in Partially Saturated Porous Media

Luong Duy Thanh ¹, Damien Jougnot ², Phan Van Do ¹, Nguyen Xuan Ca ³
and Nguyen Thi Hien ^{4,5,*}

¹ Thuyloi University, 175 Tay Son, Dong Da, Hanoi, Vietnam; thanh_lud@tlu.edu.vn (L.D.T.); phanvando@tlu.edu.vn (P.V.D.)

² Sorbonne Université, CNRS, EPHE, UMR 7619 Metis, F-75005 Paris, France; damien.jougnot@sorbonne-universite.fr

³ Department of Physics and Technology, TNU—University of Sciences, Thai Nguyen, Vietnam; canx@tnus.edu.vn

⁴ Ceramics and Biomaterials Research Group, Advanced Institute of Materials Science, Ton Duc Thang University, Ho Chi Minh City, Vietnam

⁵ Faculty of Applied Sciences, Ton Duc Thang University, Ho Chi Minh City, Vietnam

* Correspondence: nguyenthien@tdtu.edu.vn

Received: 5 April 2020; Accepted: 26 May 2020; Published: 3 June 2020



Abstract: The electrokinetics methods have great potential to characterize hydrogeological processes in porous media, especially in complex partially saturated hydrosystems (e.g., the vadose zone). The dependence of the streaming coupling coefficient on water saturation remains highly debated in both theoretical and experimental works. In this work, we propose a physically based model for the streaming potential coupling coefficient in porous media during the flow of water and air under partially saturated conditions. The proposed model is linked to fluid electrical conductivity, water saturation, irreducible water saturation, and microstructural parameters of porous materials. In particular, the surface conductivity of porous media has been taken into account in the model. In addition, we also obtain an expression for the characteristic length scale at full saturation in this work. The proposed model is successfully validated using experimental data from literature. A relationship between the streaming potential coupling coefficient and the effective excess charge density is also obtained in this work and the result is the same as those proposed in literature using different approaches. The model proposes a simple and efficient way to model the streaming potential generation for partially saturated porous media and can be useful for hydrogeophysical studies in the critical zone.

Keywords: streaming potential coupling coefficient; zeta potential; fractal; porous media

1. Introduction

During the last two decades, developments of geophysical methods for the studies of hydrosystems have led to the creation of a new scientific discipline named hydrogeophysics (see, e.g., [1–3]). Among geoelectrical methods used to study hydrogeological models in situ, the self-potential method, which consists in passively measuring the naturally occurring electrical fields at the surface or inside geological media, relies on electrokinetic coupling processes, and is therefore sensitive to fluid movements (see, e.g., [4]). For example, measurements of self-potential can be exploited for detecting and monitoring groundwater flow (see, e.g., [5–8]), geothermal areas and volcanoes (see, e.g., [9–11]), detection of contaminant plumes (see, e.g., [12,13]), monitoring water flow

in the vadose zone (see, e.g., [14–17]). Monitoring of self-potential has been proposed as a method for earthquake prediction (see, e.g., [18,19]). In hydrogeological application, self-potential measurements can be used to estimate hydrogeological parameters such as the hydraulic conductivity, the depth and the thickness of the aquifer (see, e.g., [20–22]). It is shown that the seismoelectric method has high potential to image oil and gas reservoirs or vadose zones (see, e.g., [23,24]). Furthermore, the seismo-electromagnetic method can provide supplemental information on crucial reservoir parameters such as porosity, permeability and pore fluid properties (see, e.g., [25–29]). Electrokinetics is associated with the relative movement between the mineral solid grains with charged surfaces and the pore fluid and it is linked to electrical double layer (see, e.g., [30,31]).

An important parameter of electrokinetics in porous media is the streaming potential coupling coefficient (SPCC), since this parameter controls the amount of coupling between the fluid flow and the electrical flow. Additionally, pore spaces in many subsurface porous media are saturated with water and another immiscible fluid phase such as gas, oil. Therefore, to apply electrokinetics effectively in interpretation and modeling measured data, one needs to better understand the SPCC under partially saturated conditions. There have been many studies on dependence of the SPCC of porous materials on water electrical conductivity (see, e.g., [32–35]), on temperature (see, e.g., [36,37]), on mineral compositions (see, e.g., [38,39]), on fluid pH (see, e.g., [40,41]), on hysteresis (see, e.g., [42,43]) or on porous material textures (see, e.g., [34,44]). The saturation dependence of the SPCC is not yet well understood and inconsistent in both published theoretical and experimental work as shown in Figure 1 in [45]. For example, there have been theoretical models in literature (see Table 1, for example) on the SPCC as a function of water saturation (see, e.g., [45–56]). Wurmstich and Morgan [46] and Darnet and Marquis [49] suggested that the relative SPCC should increase with decreasing water saturation. However, it was indicated that the relative SPCC varies linearly with water saturation [48]. Revil and Cerepi [50] and Saunders et al. [53] showed the decrease of the relative SPCC with decreasing water saturation. The contradiction on the saturation dependence of the SPCC is also shown in experimental work. For example, Guichet et al. [48] carried out the streaming potential measurement during drainage under gas in a water-wet sand column and observed a monotonic decrease in the relative SPCC. Nevertheless, Allegre et al. [57] observed a different behavior in which the relative SPCC initially increases before decreases with a decrease of water saturation in the similar experiments performed by [48]. In addition, a monotonic behavior of the relative SPCC in dolomite core samples was shown in [50,52]. As reported in published work, the surface conductivity plays an important role in streaming potential especially at low fluid electrical conductivity. However, it is not yet taken into consideration in available models (Table 1). Note that the non-monotonic behavior of the SPCC as a function of the water saturation was also predicted in [45,55]. Vinogradov and Jackson [58] highlighted the possible existence of hysteresis effect in the SPCC that was later studied deeper by the authors of [45].

Capillary tube models are a simple representation of the real pore space that have been used to provide valuable insight into transport in porous media (see, e.g., [55,59–65]). Thanh et al. [64] developed a model using the capillary tube model for the SPCC under saturated conditions and the model was well validated by published data. Recently, Soldi et al. [59] developed an analytical model to estimate the effective excess charge density for unsaturated flow.

In this work, we propose a physically based model for the SPCC and the relative SPCC during the flow of water and air in porous media under partially saturated conditions. Additionally, we also obtain an expression for the characteristic length scale Λ at full saturation. From the obtained expressions, we obtain the relation between the SPCC and the effective excess charge density. The proposed model for the SPCC, relative SPCC, and characteristic length scale are related to fluid electrical conductivity, specific surface conductivity, water saturation, irreducible water saturation, and microstructural parameters of porous medium. In particular, we take into account the surface conductivity of porous media in this work. The model predictions are then successfully validated by published data.

We believe that the model proposed in this work can be useful to study physical phenomena in the unsaturated zone such as infiltration, evaporation, or contaminant fluxes.

Table 1. List of the published models describing the dependence of the relative SPCC on water saturation. Notes: C_{rel} is the relative SPCC; $^a w$ is the hydrodynamic resistance factor; $^b R$ represents the excess charge in the pore water of porous media; β is the mobility of the ions and R_s is the quotient between R and S_e ; $^c S_{wn}$ and n_s are the normalized water saturation and the exponent related to the excess of mobile counterions in the electrical boundary layer, respectively; and $^d \beta$ and γ are two fitting parameters.

Expression	Reference
$C_{rel}(S_w) = \frac{1-w}{\sigma_r(S_w)}$	[46] ^a
$C_{rel}(S_w) = \frac{k_r}{\sigma_r(S_w)}$	[47]
$C_{rel}(S_w) = S_w$	[48]
$C_{rel}(S_w) = \frac{1}{\sigma_r(S_w)}$	[49]
$C_{rel}(S_w) = \frac{\beta_{(+)}(\sqrt{R^2+1}+R)+\beta_{(-)}(\sqrt{R^2+1}-R)}{\beta_{(+)}(\sqrt{R^2+1}+R_s)+\beta_{(-)}(\sqrt{R^2+1}-R_s)}$	[50] ^b
$C_{rel}(S_w) = \frac{k_r}{S_w \sigma_r(S_w)}$	[51,52]
$C_{rel}(S_w) = S_w^{n_s}$	[53] ^c
$C_{rel}(S_w) = \frac{S_e}{\sigma_r(S_w)}$	[54,59]
$C_{rel}(S_w) = S_e[1 + \beta(1 - S_e)^\gamma]$	[66] ^d

2. Theory

The streaming current in porous media is generated by the relative movement between solid grains and the pore water under a pressure difference across the porous media and is directly related to the existence of an electric double layer (EDL) at the interface between the water and solid surfaces (see, e.g., [30]). This streaming current is counterbalanced by a conduction current, leading to a so-called streaming potential. In other words, the electric current and the water flow are coupled in porous media. Therefore, the water flowing through porous media creates a streaming potential (see, e.g., [67]). The SPCC under steady state conditions is defined when the total current density is zero as (see, e.g., [68,69])

$$C_S = \frac{\Delta V}{\Delta P}, \tag{1}$$

where ΔV (V) is the generated voltage (i.e., streaming potential) and ΔP (Pa) is the applied fluid pressure difference across a porous material. There are two key expressions for the SPCC in porous media that can be found in literature. The classical one is called Helmholtz–Smoluchowski (HS) equation that links the SPCC with the zeta potential at the solid-liquid interface and fluid properties [70]. The HS equation at fully saturated conditions is given by

$$C_S^{sat} = \frac{\epsilon_r \epsilon_0 \zeta}{\eta \sigma_w}, \tag{2}$$

where ϵ_r (no units) is the relative permittivity of the fluid, ϵ_0 (F/m) is the dielectric permittivity in vacuum, η (Pa s) is the dynamic viscosity of the fluid, ζ (V) is the zeta potential, and σ_w (S/m) is the pore fluid electrical conductivity. This simple formulation predicts well the electrokinetic coupling for any kind of geometry (capillary, sphere, or porous media) as long as the surface conductivity can be neglected (see, e.g., [71,72]). Note that numerous experimental results on the SPCC were reported in literature using Equation (2) for capillaries (see, e.g., [73]), glass beads (see, e.g., [74–76]) and sandstones (see, e.g., [32,33,74,75,77–79]). The modified HS equation was expanded from the classical HS equation

when one considers the surface conductivity of solid surfaces (see, e.g., [31,44]). The modified HS equation is given by

$$C_S^{sat} = \frac{\epsilon_r \epsilon_0 \zeta}{\eta (\sigma_w + 2 \frac{\Sigma_s}{\Lambda})}. \quad (3)$$

Σ_s (S) the specific surface conductance and Λ (m) is a characteristic length scale that describes the size of the pore network and is the so-called “lambda parameter” or Johnson length [80].

Beside the HS equation or modified HS equation, the SPCC can be expressed via the effective excess charge density dragged by the water in pores of porous materials as follows (see, e.g., [51,81–84]),

$$C_S^{sat} = - \frac{k_o \widehat{Q}_V}{\eta \sigma}. \quad (4)$$

where \widehat{Q}_V (C/m³), k_o (m²), and σ (S/m) are the effective excess charge density, permeability, and electrical conductivity of porous media at saturation, respectively.

As mentioned above, under partially saturated conditions, the SPCC is a function of water saturation S_w . Therefore, one can write $C_S = C_S(S_w)$. The relative SPCC at water saturation S_w is defined as (e.g., [48,50,51])

$$C_{rel} = \frac{C_S(S_w)}{C_S^{sat}}. \quad (5)$$

In the following subsections, we present the electrokinetic properties at microscale (for one single capillary, denoted “ r ”) and macroscale (for the representative elementary volume, denoted “REV”).

2.1. Pore Scale

The electrokinetic behaviour of a capillary is now considered. Under a thin double layer assumption in which the thickness of the double layer is much smaller than the pore size and that is normally valid in most natural systems (see, e.g., [72]), the streaming current in a water occupied capillary tube of radius r (m) due to charge transport by water is given by (see, e.g., [60])

$$i_s(r) = - \frac{\pi \epsilon_r \epsilon_0 \zeta}{\eta} \frac{\Delta P}{L_\tau} r^2, \quad (6)$$

where ΔP (Pa) is the pressure difference across the capillary and L_τ (m) is the real length of the tortuous capillary (see Figure 1). Because the length of the porous media L_o (m) is related to the real length of the tortuous capillary L_τ by the relation $L_\tau = \tau L_o$ in which τ (no units) is the tortuosity of the capillary (see, e.g., [85]). Note that the length of the capillaries in this work is assumed to be independent of the capillary radius and therefore τ is the same for all capillaries (see, e.g., [54]). Equation (6) is now rewritten as

$$i_s(r) = - \frac{\pi \epsilon_r \epsilon_0 \zeta}{\eta} \frac{\Delta P}{L_o \tau} r^2. \quad (7)$$

The conduction current in the water occupied capillary tube under an electrical potential difference (ΔV) is given by

$$i_c(r) = G_{tube} \Delta V, \quad (8)$$

where G_{tube} (S) is the electrical conductance of the water occupied capillary. The electrical conductivity of a single capillary is given by the sum of the bulk and surface electrical conductivities. Note that the capillary may be occupied by either water or air. In capillaries occupied by water, surface conductivity occurs only at the interface between water and the solid, in which case Σ_s (S) denotes the specific surface conductance of this interface. In capillaries occupied by air, surface conductivity again occurs at the interface between a thin wetting phase layer (i.e., an irreducible water film) and the solid.

Consequently, in capillaries occupied by air, Σ_{sa} (S) denotes the specific surface conductance due to solid-water interfaces [54,61]. Therefore, Equation (8) is given by

$$i_c(r) = \begin{cases} \left[\frac{\sigma_w \pi r^2}{L_o \tau} + \frac{\Sigma_s 2\pi r}{L_o \tau} \right] \Delta V & \text{for a water occupied capillary} \\ \frac{\Sigma_{sa} 2\pi r}{L_o \tau} \Delta V & \text{for an air occupied capillary} \end{cases} \quad (9)$$

2.2. REV Scale

In order to develop the model for the SPCC under partially saturated conditions, we consider a representative elementary volume (REV) of a porous medium as a cube with a length L_o (see Figure 1). As stated in literature (see, e.g., [86–88]), a porous medium exhibits fractal properties and can be conceptualized as a bundle of tortuous capillaries with different sizes from a minimum pore radius r_{min} (m) to a maximum pore radius r_{max} (m). It has been proved that the number of pores with radius from r to $r + dr$ in porous media is given by (see, e.g., [64,88])

$$-dN = Dr_{max}^D r^{-D-1} dr, \quad (10)$$

where D (no units) is the fractal dimension for pore space. The negative sign implies that the number of pores decreases with the increase of pore size. Note that this is an equivalent pore size distribution that allows to reproduce the behavior of real porous media by simplifying the complexity of real pore networks. The pore fractal dimension D can be determined by a box-counting method (see, e.g., [88,89]). Additionally, D can also be estimated from the following relation (see, e.g., [88,89]),

$$D = 2 - \frac{\ln \phi}{\ln \alpha}, \quad (11)$$

where ϕ (no units) is the porosity of porous media and $\alpha = r_{min}/r_{max}$ (no units).

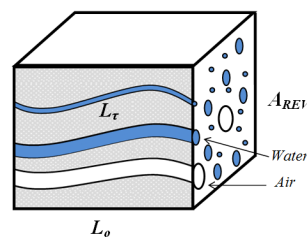


Figure 1. Conceptual model of a porous medium as a bundle of capillaries following a fractal distribution. At a given capillary pressure, the capillary is either filled by water or by air depending on its radius.

We consider the REV under at varying saturation conditions. Then, contribution to the water flow depends on the effective saturation that is given by

$$S_e = \frac{S_w - S_{wirr}}{1 - S_{wirr}}, \quad (12)$$

where S_w (no units) and S_{wirr} (no units) are the water saturation and irreducible water saturation, respectively.

We assume that the REV is initially fully saturated and then drained when it experiences a pressure head h (m). For a capillary tube, the pore radius r_h (m) is linked to the pressure head h by [90]

$$h = \frac{2T_s \cos \beta}{\rho_w g r_h}, \quad (13)$$

where T_s (N/m) is the fluid surface tension, β ($^\circ$) is the contact angle, ρ_w (kg/m^3) is the fluid density, and g (m/s^2) is the acceleration due to gravity. A capillary becomes fully desaturated if its radius r (m) is greater than the radius r_h given by Equation (13). Therefore, it is reasonable to assume that capillaries with radii r between r_{min} and r_h will remain fully saturated.

For porous media containing only large and regular pores, the irreducible water saturation can often be neglected. For porous media containing small pores, the irreducible water saturation can be quite significant. This amount of water is taken into account in the model by setting irreducible water radius of capillaries r_{wirr} (m). Consequently, the following assumptions are made in this work; (1) for $r_{min} \leq r \leq r_{wirr}$, the capillaries are occupied by water and are immobile (i.e., no film flow). Therefore, water does not contribute to the streaming current. However, water is electrically conductive, so it contributes to the conduction current. (2) For $r_{wirr} < r \leq r_h$, the capillaries are occupied by water that is mobile, so they contribute to both the streaming current and the conduction current. (3) For $r_h < r \leq r_{max}$, the capillaries are occupied by air, so does not contribute to the streaming current but contribute to the conduction current. In this work, film bound water, which adheres to the pore wall because of the molecular forces acting on the hydrophilic rock surface, in the capillaries with radius greater than r_{wirr} is ignored in water saturation calculations. Therefore, the water saturation is defined as

$$S_w = \frac{\int_{r_{min}}^{r_h} \pi r^2 L_\tau (-dN)}{\int_{r_{min}}^{r_{max}} \pi r^2 L_\tau (-dN)} = \frac{r_h^{2-D} - r_{min}^{2-D}}{r_{max}^{2-D} - r_{min}^{2-D}} \tag{14}$$

The irreducible water saturation is determined as

$$S_{wirr} = \frac{\int_{r_{min}}^{r_{wirr}} \pi r^2 L_\tau (-dN)}{\int_{r_{min}}^{r_{max}} \pi r^2 L_\tau (-dN)} = \frac{r_{wirr}^{2-D} - r_{min}^{2-D}}{r_{max}^{2-D} - r_{min}^{2-D}} \tag{15}$$

From Equations (14) and (15), one has

$$r_h = r_{max} \left[\alpha^{2-D} + S_w (1 - \alpha^{2-D}) \right]^{\frac{1}{2-D}}, \tag{16}$$

and

$$r_{wirr} = r_{max} \left[\alpha^{2-D} + S_{wirr} (1 - \alpha^{2-D}) \right]^{\frac{1}{2-D}} \tag{17}$$

where $\alpha = r_{min}/r_{max}$.

The streaming current through the REV is the sum of the streaming currents over all water occupied capillaries with radius between r_{wirr} and r_h and given by

$$\begin{aligned} I_s &= \int_{r_{wirr}}^{r_h} i_s(r) (-dN) = \\ &= - \int_{r_{wirr}}^{r_h} \frac{\pi \epsilon_r \epsilon_0 \zeta}{\eta} \frac{\Delta P}{L_0 \tau} D r_{max}^D r^{1-D} dr = \\ &= - \frac{\pi \epsilon_r \epsilon_0 \zeta}{\eta} \frac{\Delta P}{L_0 \tau} \frac{D}{2-D} r_{max}^D (r_h^{2-D} - r_{wirr}^{2-D}). \end{aligned} \tag{18}$$

The conduction current through the REV is given by

$$\begin{aligned} I_c &= \int_{r_{min}}^{r_h} i_c(r) (-dN) dr + \int_{r_h}^{r_{max}} i_c(r) (-dN) dr = \\ &= \int_{r_{min}}^{r_h} \Delta V \left[\frac{\sigma_w \pi r^2}{L_0 \tau} + \frac{\Sigma_s 2 \pi r}{L_0 \tau} \right] (-dN) dr + \int_{r_h}^{r_{max}} \Delta V \frac{\Sigma_{sa} 2 \pi r}{L_0 \tau} (-dN) dr. \end{aligned} \tag{19}$$

Evaluating integrals in Equation (19) yields

$$I_c = \frac{\Delta V D \tau r_{max}^D}{L_o \tau} \left[\frac{\sigma_w (r_h^{2-D} - r_{min}^{2-D})}{2-D} + \frac{2\Sigma_s (r_h^{1-D} - r_{min}^{1-D})}{1-D} + \frac{2\Sigma_{sa} (r_{max}^{1-D} - r_h^{1-D})}{1-D} \right]. \tag{20}$$

Under steady-state conditions, the total streaming current I_s (A) is equal to the total conduction current I_c (A) through the REV in magnitude. Therefore, the following is obtained,

$$I_s = -I_c. \tag{21}$$

Combining Equations (18), (20), and (21) yields

$$\Delta V = \frac{\epsilon_r \epsilon_0 \zeta \Delta P \frac{(r_h^{2-D} - r_{wirr}^{2-D})}{2-D}}{\eta \left[\frac{\sigma_w (r_h^{2-D} - r_{min}^{2-D})}{2-D} + \frac{2\Sigma_s (r_h^{1-D} - r_{min}^{1-D})}{1-D} + \frac{2\Sigma_{sa} (r_{max}^{1-D} - r_h^{1-D})}{1-D} \right]} \tag{22}$$

The SPCC at saturation is defined as

$$C_S = \frac{\Delta V}{\Delta P} = \frac{\epsilon_r \epsilon_0 \zeta \frac{(r_h^{2-D} - r_{wirr}^{2-D})}{2-D}}{\eta \left[\frac{\sigma_w (r_h^{2-D} - r_{min}^{2-D})}{2-D} + \frac{2\Sigma_s (r_h^{1-D} - r_{min}^{1-D})}{1-D} + \frac{2\Sigma_{sa} (r_{max}^{1-D} - r_h^{1-D})}{1-D} \right]} \tag{23}$$

Substituting Equations (16) and (17) into Equation (23) and doing some arrangements, the following is obtained,

$$C_S(S_w) = \frac{\epsilon_r \epsilon_0 \zeta (S_w - S_{wirr})}{\eta \left[\sigma_w S_w + \frac{2\Sigma_s}{r_{max}} \frac{2-D}{1-D} \frac{[(S_w(1-\alpha^{2-D}) + \alpha^{2-D})^{\frac{1-D}{2}} - \alpha^{1-D}]}{1-\alpha^{2-D}} + \frac{2\Sigma_{sa}}{r_{max}} \frac{2-D}{1-D} \frac{[1 - (S_w(1-\alpha^{2-D}) + \alpha^{2-D})^{\frac{1-D}{2}}]}{1-\alpha^{2-D}} \right]} \tag{24}$$

The wetting layer of water contributes to the surface electrical conductivity even in capillaries occupied by air. Following the work in [54], we assume that the presence of air does not modify surface conductivity at the solid water interface and $\Sigma_{sa} = \Sigma_s$. Consequently, Equation (24) becomes

$$C_S(S_w) = \frac{\epsilon_r \epsilon_0 \zeta (S_w - S_{wirr})}{\eta \left[\sigma_w S_w + \frac{2\Sigma_s}{r_{max}} \frac{2-D}{1-D} \frac{1-\alpha^{1-D}}{1-\alpha^{2-D}} \right]} \tag{25}$$

Equation (25) indicates that the SPCC under partially saturated conditions is related to the zeta potential, the fluid relative permittivity, viscosity, water saturation, irreducible water saturation, fluid electrical conductivity, and the surface conductance at the solid water interface. Additionally, Equation (25) is related to the microstructural parameters of a porous medium (D, α, r_{max}).

In case of full saturation and zero irreducible water saturation ($S_w = 1$ and $S_{wirr} = 0$), Equation (25) reduces to

$$C_S(S_w = 1) = \frac{\epsilon_r \epsilon_0 \zeta}{\eta \left[\sigma_w + \frac{2\Sigma_s}{r_{max}} \frac{2-D}{1-D} \frac{1-\alpha^{1-D}}{1-\alpha^{2-D}} \right]} \tag{26}$$

Equation (26) has been well validated by the authors of [64] for consolidated porous samples. Note that Equation (26) has the similar form as proposed by Morgan et al. [68] or Waxman and Smits [91]:

$$C_S(S_w = 1) = \frac{\epsilon_r \epsilon_0 \zeta}{\eta [\sigma_w + F\sigma_s]}, \tag{27}$$

where F is the formation factor and σ_s is the surface conductivity.

In the case of zero irreducible water saturation and negligible surface conductivity ($S_{wirr} = 0$ and $\Sigma_s = 0$), Equation (25) reduces to the HS equation (see Equation (2))

$$C_S(S_w) = \frac{\epsilon_r \epsilon_0 \zeta}{\eta \sigma_w} \tag{28}$$

Equation (28) indicates that the SPCC does not depend on water saturation in this very specific case (i.e., $S_{wirr} = 0$ and $\Sigma_s = 0$). This prediction is the same as that stated by [54] (see his Figure 3a).

2.3. Relative Streaming Potential Coupling Coefficient

From Equation (25), the relative SPCC is obtained as

$$C_{rel} = \frac{C_S(S_w)}{C_S(S_w = 1)} = \frac{\frac{S_w - S_{wirr}}{1 - S_{wirr}}}{\left[\frac{\sigma_w S_w + \frac{2\Sigma_s}{r_{max}} \frac{2-D}{1-D} \frac{1-\alpha^{1-D}}{1-\alpha^{2-D}}}{\left[\sigma_w + \frac{2\Sigma_s}{r_{max}} \frac{2-D}{1-D} \frac{1-\alpha^{1-D}}{1-\alpha^{2-D}} \right]} \right]} \tag{29}$$

For negligible surface conductivity, Equation (29) becomes

$$C_{rel} = \frac{(S_w - S_{wirr})}{(1 - S_{wirr}) S_w} = \frac{S_e}{S_w} \tag{30}$$

Equations (29) and (30) indicate the dependence of C_{rel} (no units) on water saturation S_w (no units). In addition, Equation (30) shows that when the surface conductivity is negligible, C_{rel} only depends on S_w and S_{wirr} (no units) regardless of σ_w (S/m), D (no units), r_{max} (no units), and α (no units).

2.4. The Relation Between SPCC and Effective Excess Charge Density

The effective excess charge density \hat{Q}_v^{REV} (C/m³) carried by the water flow in the REV is calculated based on the same approach proposed by [59,92]

$$\hat{Q}_v^{REV} = \frac{1}{v_D A_{REV}} \int_{r_{wirr}}^{r_h} \hat{Q}_v^r \bar{v}(r) \pi r^2 (-dN), \tag{31}$$

where v_D (m/s) is the Darcy velocity, A_{REV} (m²) is the cross-sectional area of the REV, \hat{Q}_v^r (C/m³) is the effective excess charge density carried by the water flow in a single water occupied capillary of radius r (m), and \bar{v} (m/s) is the average velocity in the capillary. As shown by [59], v_D is given as

$$v_D = \frac{\Delta P k k_{rel}}{\eta L_o}, \tag{32}$$

where k (m²) and k_{rel} (no units) are the permeability and relative permeability of the REV, respectively. Under the thin EDL assumption, \hat{Q}_v^r is given by [92]

$$\hat{Q}_v^r = -\frac{8\epsilon_r \epsilon_0 \zeta}{r^2} \tag{33}$$

Additionally, \bar{v} is given by (see, e.g., [59])

$$\bar{v}(r) = \frac{\Delta P r^2}{8\eta \tau L_o} \tag{34}$$

Substituting Equations (32)–(34) into Equation (31) and doing some arrangements, one obtains

$$\hat{Q}_v^{REV} = -\frac{\epsilon_r \epsilon_0 \zeta}{\tau k k_{rel}} \frac{\pi D}{(2 - D) A_{REV}} r_{max}^D r_{max}^{2-D} (S_w - S_{wirr}) (1 - \alpha^{2-D}). \tag{35}$$

In addition, the electrical conductivity of the REV at saturation is calculated as

$$\sigma = \frac{L_o}{A_{REV}R_{REV}}, \tag{36}$$

where R_{REV} (Ω) is the resistance of the REV that can be deduced from Equation (20) using Ohm's law:

$$\frac{1}{R_{REV}} = \frac{I_c}{\Delta V} = \frac{D\pi r_{max}^D}{L_o\tau} \left[\frac{\sigma_w(r_h^{2-D} - r_{min}^{2-D})}{2-D} + \frac{2\Sigma_s(r_h^{1-D} - r_{min}^{1-D})}{1-D} + \frac{2\Sigma_{sa}(r_{max}^{1-D} - r_h^{1-D})}{1-D} \right]. \tag{37}$$

Using $\Sigma_s = \Sigma_{sa}$ and applying the same above mentioned approach, Equation (37) is rewritten as

$$\frac{1}{R_{REV}} = \frac{D\pi r_{max}^D r_{max}^{2-D} (1 - \alpha^{2-D})}{L_o\tau(2-D)} \left[\sigma_w S_w + \frac{2\Sigma_s}{r_{max}} \frac{2-D}{1-D} \frac{1 - \alpha^{1-D}}{1 - \alpha^{2-D}} \right]. \tag{38}$$

Combining Equations (36) and (38), the following is obtained,

$$\sigma(S_w) = \frac{\pi D r_{max}^2 (1 - \alpha^{2-D})}{A_{REV}\tau(2-D)} \left[\sigma_w S_w + \frac{2\Sigma_s}{r_{max}} \frac{2-D}{1-D} \frac{1 - \alpha^{1-D}}{1 - \alpha^{2-D}} \right]. \tag{39}$$

From Equations (25), (35), and (39), one has

$$C_S(S_w) = -\frac{\hat{Q}_v^{REV}(S_w) k k_{rel}(S_w)}{\eta\sigma(S_w)}. \tag{40}$$

Equation (40) is the same as that reported in literature using different approaches such as the volume-averaging upscaling (see, e.g., [51,55,83]). However, in this work, we obtain that based on the fractal theory for porous media and the capillary tube model.

From Equation (39), the relative electrical conductivity is obtained as

$$\sigma_{rel}(S_w) = \frac{\sigma(S_w)}{\sigma(S_w = 1)} = \frac{\sigma_w S_w + \frac{2\Sigma_s}{r_{max}} \frac{2-D}{1-D} \frac{1 - \alpha^{1-D}}{1 - \alpha^{2-D}}}{\sigma_w + \frac{2\Sigma_s}{r_{max}} \frac{2-D}{1-D} \frac{1 - \alpha^{1-D}}{1 - \alpha^{2-D}}}. \tag{41}$$

Comparing Equations (29) and (41) yields the following

$$C_{rel} = \frac{S_e}{\sigma_{rel}(S_w)}. \tag{42}$$

Equation (42) is exactly the same as that proposed by the authors of [54,59].

2.5. Johnson Length

Comparing Equations (3) and (26), a new expression for the characteristic length scale (Johnson length) Λ (m) under fully saturated conditions is obtained as

$$\Lambda = r_{max} \frac{(1-D)(1 - \alpha^{2-D})}{(2-D)(1 - \alpha^{1-D})} = r_{max} \frac{(1-D)(1 - \phi)}{(2-D)(1 - \alpha^{1-D})}. \tag{43}$$

It should be noted that $\alpha^{2-D} = \phi$.

There have been published models relating the Λ (m) to the grain diameter d (m). One is presented by [93,94]

$$\Lambda = \frac{d}{2m(F-1)} \approx \frac{d}{2mF}, \tag{44}$$

where F (no units) is the formation factor, m (no units) is the cementation exponent of porous media. For spherical grain based samples, m is stated to be 1.5 (see, e.g., [95]).

Equation (43) is related to microstructural properties of porous materials (D , ϕ , α , r_{max}). Therefore, it indicates more mechanisms affecting the Λ (m) than Equation (44). There is no empirical constants in Equation (43), but there are two in Equation (44) (F and m).

The effective pore radius is linked to the characteristic length scale by [96]

$$r_{eff} = \Lambda \sqrt{\frac{8}{a}}, \quad (45)$$

where a (no units) is a constant and normally taken as to 8/3 for spherical grain based samples [94,96]. Combining Equations (43) and (45), the r_{eff} (m) can be expressed in terms of microstructural parameters of porous materials as follows:

$$r_{eff} = r_{max} \frac{(1-D)(1-\phi)}{(2-D)(1-\alpha^{1-D})} \sqrt{\frac{8}{a}}. \quad (46)$$

Combining Equations (44) and (45), the r_{eff} (m) is expressed in terms of F and m as follows,

$$r_{eff} = \frac{d}{2m(F-1)} \sqrt{\frac{8}{a}} \approx \frac{d}{2mF} \sqrt{\frac{8}{a}}. \quad (47)$$

3. Results and Discussion

3.1. Relative Streaming Potential Coupling Coefficient

Figure 2 shows the variation of the relative SPCC with water saturation predicted from Equation (30) for three values of irreducible water saturation S_{wirr} . It is seen that C_{rel} increases with increasing water saturation S_w as observed in literature (see, e.g., [48,50,58]). When $S_{wirr} = 0$, C_{rel} is always equal 1, meaning that the SPCC does not depend on water saturation as predicted by [54]. In addition, C_{rel} is very sensitive with S_{wirr} (C_{rel} decreases with an increase of S_{irr} at the same water saturation). The reason is that at the same water saturation there are less capillaries occupied by water that is mobile for the electrokinetic effect when S_{irr} increases.

Figure 3 shows the variation of the relative SPCC (C_{rel}) with fluid electrical conductivity (σ_w) based on Equation (29) for three different values of D (1.3, 1.6, and 1.9). Input parameters for modeling are $\Sigma_s = 10 \times 10^{-9}$ S that is a typical value reported in literature (see, e.g., [97–99]), $S_{wirr} = 0.2$, $S_w = 0.3$, $r_{max} = 50.10^{-6}$ m and $\alpha = 0.01$. It is seen that the relative SPCC increases with increasing electrical conductivity at low electrical conductivity for all three values of D . However, at high fluid electrolyte conductivity ($\sigma_w \approx 1$ S/m), the relative SPCC becomes independent of D that is linked to grain texture of porous media. The reason is that at high fluid electrical conductivity the surface conductivity is negligible, the C_{rel} is now determined by Equation (30) and is independent of σ_w and D (see the dashed line in Figure 3). Additionally, it is seen that C_{rel} decreases with an increase of D at low fluid electrical conductivity.

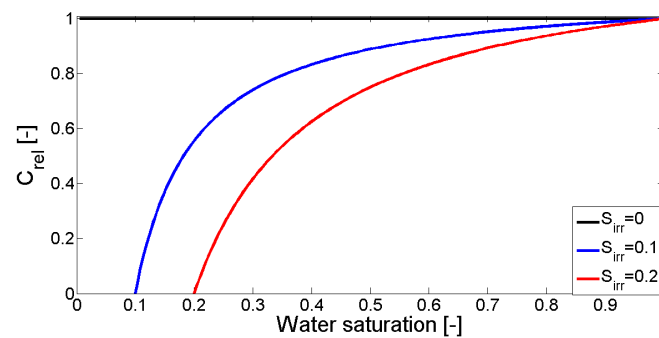


Figure 2. The variation of the relative SPCC with water saturation for the zero surface conductivity ($\Sigma_s = 0$) predicted from Equation (30) at three values of $S_{w,irr}$ (0, 0.1, and 0.2).

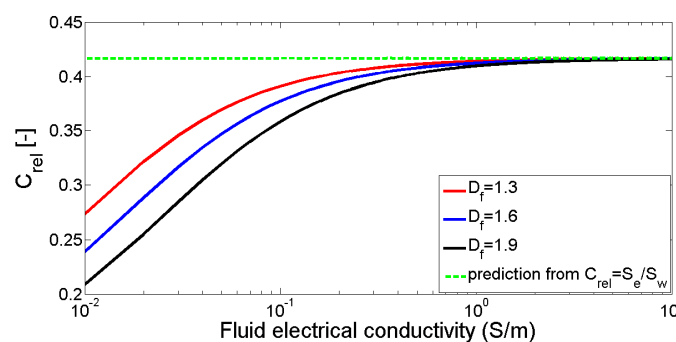


Figure 3. The variation of the relative SPCC with fluid electrical conductivity predicted from Equation (29) for three values of D : 1.3, 1.6, and 1.9 (see the solid lines) with $\Sigma_s = 10 \times 10^{-9}$ S, $S_{w,irr} = 0.2$, $S_w = 0.3$, $r_{max} = 50 \cdot 10^{-6}$ m and $\alpha = 0.01$. The dashed line is predicted from Equation (30).

If pore size distribution is not known, one can estimate the maximum pore radius with the knowledge of the mean grain diameter d of porous materials as [100]

$$r_{max} = \frac{d}{8} \left[\sqrt{\frac{2\phi}{1-\phi}} + \sqrt{\frac{\phi}{1-\phi}} + \sqrt{\frac{\pi}{4(1-\phi)}} - 1 \right], \tag{48}$$

Equation (48) has been justified by a good agreement with experimental data as shown in the recent work (see, e.g., [64,65]). Equation (48) will be used to determine r_{max} in later modelings.

Vinogradov and Jackson [58] measured C_{rel} as a function of S_w for the St. Bees sample saturated with brine/nitrogen and brine/undecane (see symbols in Figure 4). When the sample is saturated with brine/nitrogen, C_{rel} is observed to approach zero at the irreducible water saturation ($S_{w,irr} = 0.3$) as indicated in Figure 4a. The brine used in [58] was a simple 0.01 M solution of NaCl. Therefore, to estimate the fluid electrical conductivity, we use the relation $\sigma_w = 10 \times C_f = 0.1$ S/m for a NaCl solution in the range of electrolyte concentration C_f between 10^{-6} M and 1 M temperature between 15 °C and 25 °C [101]. With fluid electrical conductivity of 0.1 S/m, the surface conductivity is not safely neglected for the same system of the sample and fluid as reported in [33] in which the surface conductivity is negligible for σ_w larger than 1 S/m. Therefore, we use Equation (29) to reproduce the experimental data in Figure 4a (see the solid line) with $S_{w,irr} = 0.3$, $d = 130 \mu\text{m}$, $\phi = 0.19$, $\sigma_w = 0.1$ S/m which are obtained from [58], $\Sigma_s = 10 \times 10^{-9}$ S (typical value for silica based rocks in contact with NaCl solutions) and $\alpha = 0.01$ (best fit). A good agreement between the model and experimental data is observed. Note that D is determined from Equation (11) with the knowledge of ϕ and α ; r_{max} is determined from Equation (48) with the knowledge of ϕ and d .

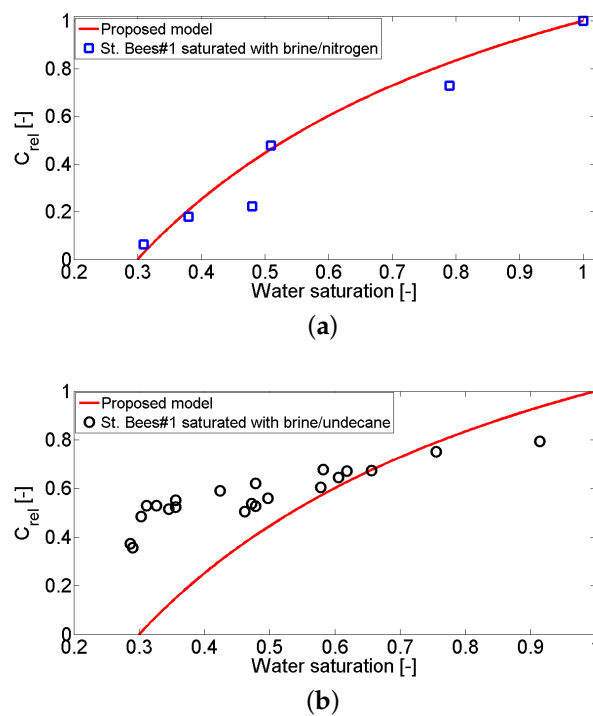


Figure 4. The variation of the relative SPCC with water saturation for St. Bees#1 (see symbols) taken from [58]: (a) saturated with brine/nitrogen; (b) saturated with brine/undecane. The solid lines are predicted from Equation (29) with $S_{w,irr} = 0.3$, $d = 130 \mu\text{m}$, $\phi = 0.19$, $\sigma_w = 0.1 \text{ S/m}$, $\Sigma_s = 10 \times 10^{-9} \text{ S}$ and $\alpha = 0.01$.

However, Vinogradov and Jackson [58] observed that the relative SPCC gets the non-zero value at the irreducible water saturation as shown in Figure 4b for brine/undecane. That observation may be due to the movement of brine along with the undecane within the wetting layers of the pores [102]. That effect is important at low brine saturation (wetting phase). The small volumes of flowing brine are hard to be measured and therefore the brine saturation seems to be unchanging. However, the brine contains a very high density of excess electrical charge [44,58]. Consequently, the streaming current is considerable, leading to a non-zero streaming potential at the irreducible water saturation. One can note that the proposed model is valid for porous media saturated by water (brine)/air (nitrogen). The reason is that the model is developed based on assumption of water-wet capillaries saturated with water and a nonwetting phase such as air as mentioned in Section 2.

Figure 5 shows experimental data of C_{rel} as a function of S_w for a sand column saturated with brine/argon (see symbols) obtained from [48]. The experimental data is explained by the model given by Equation (29) (see the lines). To see how sensitive the model is with Σ_s and α , three different values of Σ_s (0 , $30 \times 10^{-9} \text{ S}$ and $60 \times 10^{-9} \text{ S}$) and three different values of α (0.01 , 0.001 , and 0.0001) are applied for modeling (see Figure 5a,b, respectively). Input parameters for modeling are $S_{w,irr} = 0.41$, $d = 300 \mu\text{m}$, $\phi = 0.4$, $\sigma_w = 0.01 \text{ S/m}$ that are taken from [48]. In Figure 5a, $\alpha = 0.01$ is used and in Figure 5b, $\Sigma_s = 30 \times 10^{-9} \text{ S}$ is used. It is seen that the model is very sensitive with Σ_s and α . A good agreement between the experimental data and the model is obtained with $\alpha = 0.01$ and $\Sigma_s = 30 \times 10^{-9} \text{ S}$. Note that $\alpha = 0.01$ are normally relevant for unconsolidated samples of sand grains (see, e.g., [64,65,88]) and $\Sigma_s = 30 \times 10^{-9} \text{ S}$ is of the same order of magnitude as those reported in published work (see, e.g., [76,97,103]).

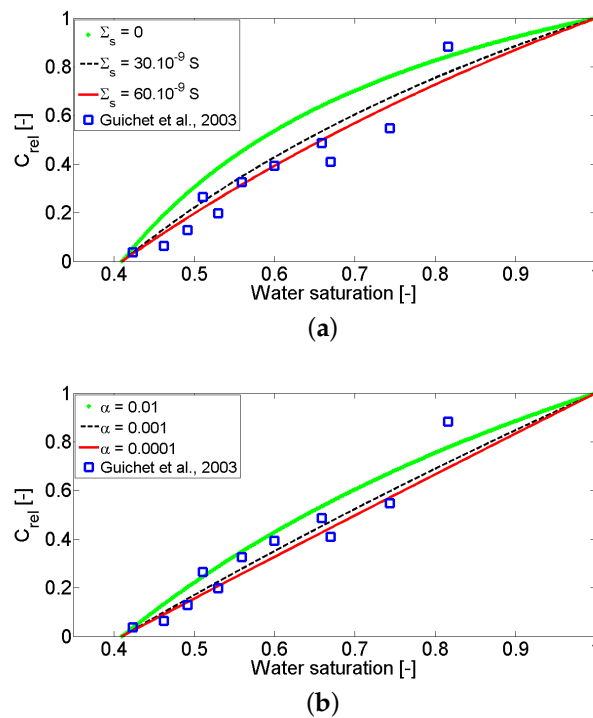


Figure 5. The variation of the relative SPCC with water saturation for a sand column saturated with brine/argon (see symbols) taken from the work in [48]. The lines are predicted from Equation (29) for three different values of $\Sigma_s = 0, 30 \times 10^{-9}$ S and 60×10^{-9} S (a) and three different values of $\alpha = 0.01, 0.001$ and 0.0001 (b). Input parameters for modeling are $S_{wirr} = 0.41, d = 300 \mu\text{m}, \phi = 0.4, \sigma_w = 0.01$ S/m that are reported by [48]. In panel (a), $\alpha = 0.01$ is used and in Figure 5b, $\Sigma_s = 30 \times 10^{-9}$ S is used.

Figure 6 shows experimental data of C_{rel} as a function of S_w for the samples E39 and E3 saturated with brine/nitrogen obtained from the work in [50] and the sample of Brauvilliers limestone saturated with brine/nitrogen obtained from the work in [83] (see symbols in Figure 6a,b, respectively). Equation (30) is applied to explain the experimental data because the fluid electrical conductivities in both cases are reported to be large enough to ignore the surface conductivity ($\sigma_w = 0.93$ S/m and 1.33 S/m). The solid lines are obtained from Equation (30) in which $S_{wirr} = 0.4$ and $S_{wirr} = 0.29$ are reported by the authors of [50,83], respectively. It is seen that the model predictions are in good agreement with the published data.

Figure 7 shows the dependence of the SPCC on the fluid electrical conductivity for two glass bead packs (S1a with $d = 56 \mu\text{m}$ and S5 with $d = 512 \mu\text{m}$) saturated with NaCl solutions (see symbols) taken from [99] at full saturation. Equation (26) is used to explain the observed behavior, in which ϕ is taken as 0.4 [99], $\Sigma_s = 10^{-9}$ S and $\alpha = 0.01$ are used for the best fit. D and r_{max} are determined in the same way as previously mentioned with the knowledge of ϕ, α and d . The dependence of the zeta potential on fluid electrical conductivity is based on the empirical expression $\zeta = -9.67 + 19.02 \log_{10}(\sigma_w)$ (mV) given by [33]. It is seen that the model can reproduce the main trend of the published data. Additionally, two empirical laws between the SPCC (mV/MPa) and electrolyte concentration C_f (mol/L) proposed by Vinogradov et al. [33] for sandstone ($C_S(S_w = 1) = -1.36C_f^{-0.9123}$) and by Cherubini et al. [104] for Carbonate rocks ($C_S(S_w = 1) = -1.41C_f^{-0.862}$) are used to reproduce the experimental data reported by [99] (see Figure 7). Recall that the relation $\sigma_w = 10C_f$ is also used to deduce C_f from σ_w . As seen in Figure 7, the empirical laws overestimate experimental data even they can explain the decrease of the SPCC with an increase of σ_w . The reason is that those laws were obtained by fitting experimental data with big data scattering (e.g., see Figure 10 of [33]). Therefore, the empirical laws may not work well for two single silica-based samples in a large range of electrical conductivity reported by [99]. In addition,

the difference in expressions proposed by the authors of [33,104] indicates that the empirical law is largely mineral-dependent.

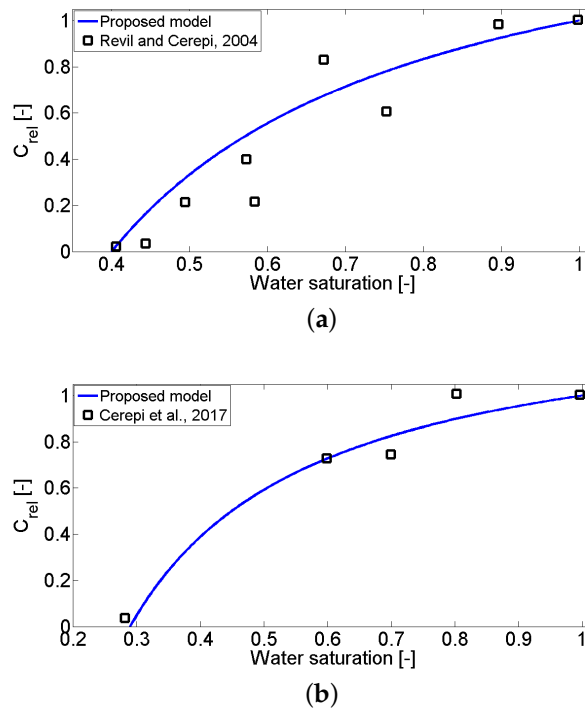


Figure 6. The variation of the relative SPCC with water saturation for (a) two dolomite core samples (E39 and E3) saturated with brine/nitrogen (see symbols) taken from the work in [50] in which $S_{wirr} = 0.4$; (b) the sample of Brauvilliers limestone saturated with brine/gas (see symbols) taken from the work in [83] in which $S_{wirr} = 0.29$. The solid lines are predicted from Equation (30).

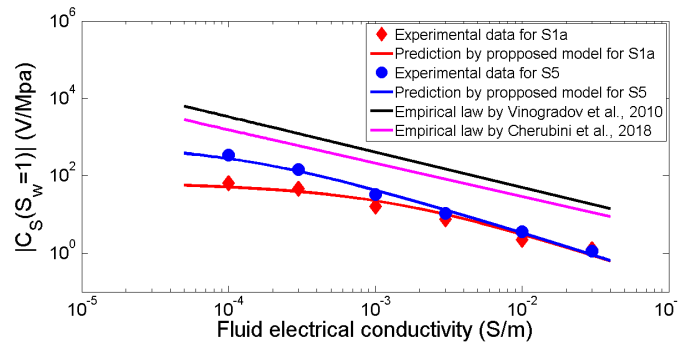


Figure 7. The variation of the SPCC at full saturation with the fluid electrical conductivity for two glass bead pack (S1a and S5) saturated with NaCl solutions (see symbols) taken from the work in [99]. The solid lines are predicted from Equation (26) and two empirical laws proposed by Vinogradov et al. [33] and by Cherubini et al. [104].

3.2. Johnson Length

Figure 8 shows the variation of the characteristic length scale with porosity predicted from Equation (46) at three different values of α (0.01, 0.025, and 0.05) for $d = 50 \times 10^{-6}$ m. It is shown that the characteristic length scale is sensitive to the porosity ϕ and the ratio α between r_{min} and r_{max} .

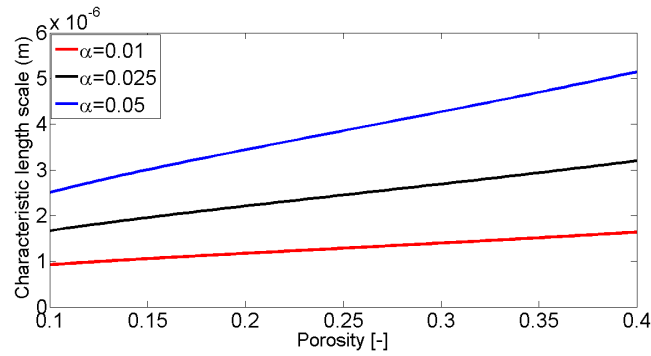


Figure 8. The variation of the characteristic length scale with porosity at three different values of α (0.01, 0.025 and 0.05) for $d = 50 \times 10^{-6}$ m.

In Figure 9, we show (a) the comparison between effective pore radii predicted from the proposed model given by Equation (46) and those predicted from Equation (47) presented by [94,96] for a set of glass bead packs (see Table 2), and (b) the comparison between effective pore radii predicted from the proposed model given by Equation (46) and those from measurements of the mercury injection capillary pressure (MICP) for the same set of samples (see Table 2). It is seen that the proposed model given by Equation (46) is very good agreement with that presented by [94,96] or experimental data from the MICP measurements. It should be noted that in Equation (46), α is taken as 0.025 due to the best fit, D and r_{max} are determined from (11) and Equation (48) as previously mentioned with the knowledge of α , ϕ and d (see Table 2). For modeling of Equation (46) and Equation (47), d and m are obtained from [94,96] and re-shown in Table 2, F is determined by the relation $F = \phi^{-m}$ [105], and a is taken as 8/3.

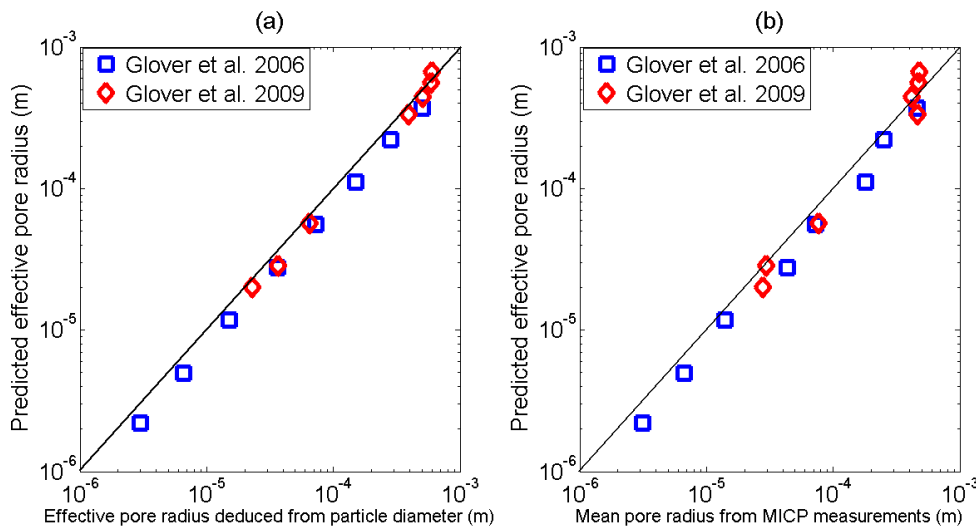


Figure 9. Comparison of predicted and measured effective pore radii for a set of glass bead packs reported in [94,96]. (a) Predicted effective pore radius given by Equation (46) against the pore radius associated with the grain diameter given by Equation (47). (b) Predicted effective pore radius given by Equation (46) against the mean pore radius from MICP measurements reported in [96].

Table 2. Properties for a set of glass bead packs reported in [94,96]. Symbols of d (μm), ϕ (no units), m (no units), and r_{mean} (μm) stand for the grain diameter, porosity, cementation exponent, and mean pore radius of glass bead samples from mercury injection capillary pressure (MICP) measurements, respectively.

Sample	d (μm)	ϕ (no units)	m (no units)	r_{mean} from MICP (μm)	Source
A	20	0.4009	1.49	3.12	[94]
B	45	0.3909	1.48	6.65	[94]
C	106	0.3937	1.50	14.04	[94]
D	250	0.3982	1.50	43.7	[94]
E	500	0.3812	1.46	72.3	[94]
F	1000	0.3954	1.47	180.2	[94]
G	2000	0.3856	1.49	252.6	[94]
H	3350	0.3965	1.48	459.3	[94]
I	3000	0.3978	1.56	463.1	[96]
J	4000	0.3854	1.55	419.7	[96]
K	5000	0.3756	1.57	476.2	[96]
L	6000	0.3566	1.62	480.0	[96]
M	256	0.3987	1.51	29.6	[96]
N	512	0.3890	1.56	76.9	[96]
O	181	0.3824	1.54	28.1	[96]

Similarly, Glover and Dery (2010) [76] applied Equation (47) for a set of glass bead packs to obtain the effective pore radii of the samples (see his Table 1). The properties and the effective pore radii obtained by [76] for all samples are re-shown in Table 3. From that, the variation of effective pore radii with grain diameter is shown in Figure 10 (see symbols). The observation can be reproduced by Equation (46) (see solid line), in which α is taken as 0.025, D and r_{max} are obtained in the same manner as previously mentioned with the knowledge of α , ϕ , and d (see Table 3). It is seen that the model provides a fairly good agreement with experimental data.

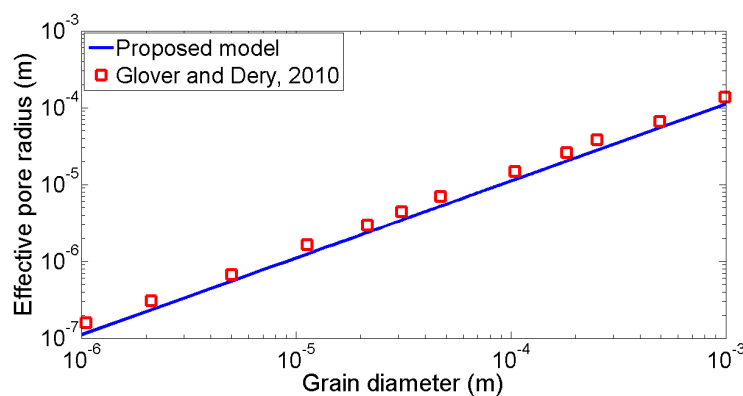


Figure 10. Comparison of measured and predicted effective pore radii for a range of glass bead packs reported by [76]. In the model: $\alpha = 0.025$, ϕ and m are reported in [76], $a = 8/3$ and $F = \phi^{-m}$.

Table 3. Properties for a set of glass bead packs reported in [76]. Symbols of d (μm), ϕ (no units), m (no units), F (no units), and r_{eff} (μm) stand for the grain diameter, porosity, cementation exponent, formation factor, and effective pore radius of the glass bead samples, respectively.

Sample	d (μm)	ϕ (no units)	m (no units)	F (no units)	r_{eff} (μm)	Source
1	1.05	0.411	1.5	3.80	0.16	[76]
2	2.11	0.398	1.5	3.98	0.31	[76]
3	5.01	0.380	1.5	4.27	0.68	[76]
4	11.2	0.401	1.5	3.94	1.64	[76]
5	21.5	0.383	1.5	4.23	2.94	[76]
6	31.0	0.392	1.5	4.07	4.40	[76]
7	47.5	0.403	1.5	3.91	7.02	[76]
8	104	0.394	1.5	4.04	14.86	[76]
9	181	0.396	1.5	4.01	26.04	[76]
10	252	0.414	1.5	3.75	38.53	[76]
11	494	0.379	1.5	4.28	66.64	[76]
12	990	0.385	1.5	4.18	136.62	[76]

4. Conclusions

We develop a physically based model for the SPCC as well as the relative SPCC during the flow of water and air in porous materials under partially saturated conditions by considering a bundle of tortuous capillaries with a fractal pore size distribution. From the obtained expressions, we obtain the familiar relation between the SPCC and the effective excess charge density that has been reported in literature using another approach. The proposed model for the SPCC and relative SPCC is related to fluid electrical conductivity, water saturation, irreducible water saturation, and microstructural parameters of porous media. In particular, the surface conductivity of porous media has been taken into account in the model. In addition, we also obtain a new expression for the characteristic length scale Λ at full saturation. The proposed model is then successfully validated using experimental data in literature. We believe that the models proposed in this work can be useful to study hydrogeological processes in the unsaturated zone such as infiltration, evaporation, or contaminant fluxes.

Author Contributions: Conceptualization, L.D.T. and D.J.; methodology, L.D.T. and D.J.; formal analysis, L.D.T., D.J., P.V.D., N.X.C. and N.T.H.; investigation, L.D.T., D.J., P.V.D., N.X.C. and N.T.H.; data curation, L.D.T., D.J., P.V.D., N.X.C. and N.T.H.; writing—original draft preparation, L.D.T. and D.J.; writing—review and editing, L.D.T., D.J., N.T.H. All authors have read and agreed to the published version of the manuscript.

Funding: This research is funded by Vietnam National Foundation for Science and Technology Development (NAFOSTED) under grant number 103.99-2019.316.

Acknowledgments: The authors strongly thank the guest editor and the three reviewers for their nice and very constructive comments.

Conflicts of Interest: The authors declare no conflict of interest.

References

1. Rubin, Y.; Hubbard, S. *Hydrogeophysics*; Springer: Berlin/Heidelberg, Germany, 2006.
2. Hubbard, S.; Linde, N. *Hydrogeophysics*. In *Treatise on Water Science*; Wilderer, P., Ed.; Academic Press: Oxford, UK, 2011.
3. Binley, A.; Hubbard, S.S.; Huisman, J.A.; Revil, A.; Robinson, D.A.; Singha, K.; Slater, L.D. The emergence of hydrogeophysics for improved understanding of subsurface processes over multiple scales. *Water Resour. Res.* **2015**, *51*, 3837–3866. [[CrossRef](#)] [[PubMed](#)]
4. Revil, A.; Jardani, A. *The Self-Potential Method: Theory and Applications in Environmental Geosciences*; Cambridge University Press: Cambridge, UK, 2013.
5. Jouniaux, L.; Pozzi, J.; Berthier, J.; Masse, P. Detection of fluid flow variations at the Nankai Trough by electric and magnetic measurements in boreholes or at the seafloor. *J. Geophys. Res.* **1999**, *104*, 29293–29309. [[CrossRef](#)]

6. Fagerlund, F.; Heinson, G. Detecting subsurface groundwater flow in fractured rock using self-potential (SP) methods. *Environ. Geol.* **2003**, *43*, 782–794. [[CrossRef](#)]
7. Titov, K.; Revil, A.; Konosavsky, P.; Straface, S.; Troisi, S. Numerical modelling of self-potential signals associated with a pumping test experiment. *Geophys. J. Int.* **2005**, *162*, 641–650. [[CrossRef](#)]
8. Aizawa, K.; Ogawa, Y.; Ishido, T. Groundwater flow and hydrothermal systems within volcanic edifices: Delineation by electric self-potential and magnetotellurics. *J. Geophys. Res.* **2009**, *114*. [[CrossRef](#)]
9. Aubert, M.; Atangana, Q.Y. Self-Potential Method in Hydrogeological Exploration of Volcanic Areas. *Groundwater* **1996**, *34*, 1010–1016. [[CrossRef](#)]
10. Finizola, A.; Lenat, N.; Macedo, O.; Ramos, D.; Thouret, J.; Sortino, F. Fluid circulation and structural discontinuities inside misti volcano (peru) inferred from self-potential measurements. *J. Volcanol. Geotherm. Res.* **2004**, *135*, 343–360. [[CrossRef](#)]
11. Mauri, G.; Williams-Jones, G.; Saracco, G. Depth determinations of shallow hydrothermal systems by self-potential and multi-scale wavelet tomography. *J. Volcanol. Geotherm. Res.* **2010**, *191*, 233–244. [[CrossRef](#)]
12. Martinez-Pagan, P.; Jardani, A.; Revil, A.; Haas, A. Self-potential monitoring of a salt plume. *Geophysics* **2010**, *75*, WA17–WA25. [[CrossRef](#)]
13. Naudet, V.; Revil, A.; Bottero, J.Y.; Bégassat, P. Relationship between self-potential (SP) signals and redox conditions in contaminated groundwater. *Geophys. Res. Lett.* **2003**, *30*. [[CrossRef](#)]
14. Doussan, C.; Jouniaux, L.; Thony, J.L. Variations of self-potential and unsaturated water flow with time in sandy loam and clay loam soils. *J. Hydrol.* **2002**, *267*, 173–185. [[CrossRef](#)]
15. Jougnot, D.; Linde, N.; Haarder, E.; Looms, M. Monitoring of saline tracer movement with vertically distributed self-potential measurements at the HOBE agricultural test site, Voulund, Denmark. *J. Hydrol.* **2015**, *521*, 314–327. [[CrossRef](#)]
16. Voytek, E.B.; Barnard, H.R.; Jougnot, D.; Singha, K. Transpiration- and precipitation-induced subsurface water flow observed using the self-potential method. *Hydrol. Process.* **2019**, *33*, 1784–1801. [[CrossRef](#)]
17. Hu, K.; Jougnot, D.; Huang, Q.; Looms, M.C.; Linde, N. Advancing quantitative understanding of self-potential signatures in the critical zone through long-term monitoring. *J. Hydrol.* **2020**, *585*, 124771. [[CrossRef](#)]
18. Pozzi, J.; Jouniaux, L. Electrical Effects Of Fluid Circulation In Sediments And Seismic Prediction. *C. R. Acad. Sci. Ser. II* **1994**, *318*, 73–77.
19. Trique, M.; Richon, P.; Perrier, F.; Avouac, J.; Sabroux, J.C. Radon emanation and electric potential variations associated with transient deformation near reservoir lakes. *Nature* **1999**, *399*, 137–141. [[CrossRef](#)]
20. Darnet, M.; Marquis, G.; Sailhac, P. Estimating aquifer hydraulic properties from the inversion of surface Streaming Potential (SP) anomalies. *Geophys. Res. Lett.* **2003**, *30*. [[CrossRef](#)]
21. Jardani, A.; Revil, A.; Boleve, A.; Crespy, A.; Dupont, J.P.; Barrash, W.; Malama, B. Tomography of the Darcy velocity from self-potential measurements. *Geophys. Res. Lett.* **2007**, *34*. [[CrossRef](#)]
22. Jouniaux, L.; Maineult, A.; Naudet, V.; Pessel, M.; Sailhac, P. Review of self-potential methods in hydrogeophysics. *C. R. Geosci.* **2009**, *341*, 928–936. [[CrossRef](#)]
23. Revil, A.; Barnier, G.; Karaoulis, M.; Sava, P.; Jardani, A.; Kulesa, B. Seismoelectric coupling in unsaturated porous media: Theory, petrophysics, and saturation front localization using an electroacoustic approach. *Geophys. J. Int.* **2013**, *196*, 867–884. [[CrossRef](#)]
24. Dupuis, J.C.; Butler, K.E.; Kepic, A.W. Seismoelectric imaging of the vadose zone of a sand aquifer. *Geophysics* **2007**, *72*, A81–A85. [[CrossRef](#)]
25. Pride, S. Governing equations for the coupled electromagnetics and acoustics of porous media. *Phys. Rev. B* **1994**, *50*, 15678–15696. [[CrossRef](#)] [[PubMed](#)]
26. Haines, S.S.; Pride, S.R. Seismoelectric numerical modeling on a grid. *Geophysics* **2006**, *71*, N57–N65. [[CrossRef](#)]
27. Jougnot, D.; Rubino, J.G.; Carbajal, M.R.; Linde, N.; Holliger, K. Seismoelectric effects due to mesoscopic heterogeneities. *Geophys. Res. Lett.* **2013**, *40*, 2033–2037. [[CrossRef](#)]
28. Smeulders, D.; Grobde, N.; Heller, H.; Schakel, M. Seismoelectric Conversion for the Detection of Porous Medium Interfaces between Wetting and Nonwetting Fluids. *Vadose Zone J.* **2014**, *13*, 1–7.
29. Bordes, C.; Sénéchal, P.; Barrière, J.; Brito, D.; Normandin, E.; Jougnot, D. Impact of water saturation on seismoelectric transfer functions: A laboratory study of coseismic phenomenon. *Geophys. J. Int.* **2015**, *200*, 1317–1335. [[CrossRef](#)]

30. Overbeek, J. Electrochemistry of the double layer. In *Colloid Science, Irreversible Systems*; Kruyt, H.R., Ed.; Elsevier: Amsterdam, The Netherlands, 1952.
31. Hunter, R.J. *Zeta Potential in Colloid Science*; Academic: New York, NY, USA, 1981.
32. Lorne, B.; Perrier, F.; Avouac, J.P. Streaming potential measurements: 1. Properties of the electrical double layer from crushed rock samples. *J. Geophys. Res.* **1999**, *104*, 17.857–17.877. [[CrossRef](#)]
33. Vinogradov, J.; Jaafar, M.Z.; Jackson, M.D. Measurement of streaming potential coupling coefficient in sandstones saturated with natural and artificial brines at high salinity. *J. Geophys. Res.* **2010**, *115*. [[CrossRef](#)]
34. Glover, P.W.J.; Walker, E.; Jackson, M. Streaming-potential coefficient of reservoir rock: A theoretical model. *Geophysics* **2012**, *77*, D17–D43. [[CrossRef](#)]
35. Luong, D.; Sprik, R. Examination of a theoretical model of streaming potential coupling coefficient. *Int. J. Geophys.* **2014**, *2014*, 471819. [[CrossRef](#)]
36. Tosha, T.; Matsushima, N.; Ishido, T. Zeta potential measured for an intact granite sample at temperatures to 200 °C. *Geophys. Res. Lett.* **2003**, *30*. [[CrossRef](#)]
37. Vinogradov, J.; Jackson, M.D. Zeta potential in intact natural sandstones at elevated temperatures. *Geophys. Res. Lett.* **2015**, *42*, 6287–6294. [[CrossRef](#)]
38. Maineult, A.; Jouniaux, L.; Bernabé, Y. Influence of the mineralogical composition on the self-potential response to advection of KCl concentration fronts through sand. *Geophys. Res. Lett.* **2006**, *33*. [[CrossRef](#)]
39. Thanh, L.D.; Sprik, R. Zeta potential in porous rocks in contact with monovalent and divalent electrolyte aqueous solutions. *Geophysics* **2016**, *81*, D303–D314. [[CrossRef](#)]
40. Guichet, X.; Jouniaux, L.; Catel, N. Modification of streaming potential by precipitation of calcite in a sand–water system: Laboratory measurements in the pH range from 4 to 12. *Geophys. J. Int.* **2006**, *166*, 445–460. [[CrossRef](#)]
41. Walker, E.; Glover, P.W.J. Measurements of the Relationship Between Microstructure, pH, and the Streaming and Zeta Potentials of Sandstones. *Transp. Porous Media* **2018**, *121*, 183–206. [[CrossRef](#)] [[PubMed](#)]
42. Allegre, V.; Maineult, A.; Lehmann, F.; Lopes, F.; Zamora, M. Self-potential response to drainage–imbibition cycles. *Geophys. J. Int.* **2014**, *197*, 1410–1424. [[CrossRef](#)]
43. Soldi, M.; Guarracino, L.; Jougnot, D. An effective excess charge model to describe hysteresis effects on streaming potential. *J. Hydrol.* **2020**, 124949. [[CrossRef](#)]
44. Revil, A.; Pezard, P.A.; Glover, P.W.J. Streaming potential in porous media 1. Theory of the zeta potential. *J. Geophys. Res.* **1999**, *104*, 20021–20031. [[CrossRef](#)]
45. Zhang, J.; Vinogradov, J.; Leinov, E.; Jackson, M.D. Streaming potential during drainage and imbibition. *J. Geophys. Res. Solid Earth* **2017**, *122*, 4413–4435. [[CrossRef](#)]
46. Wurmstich, B.; Morgan, F.D. Modeling of streaming potential responses caused by oil well pumping. *Geophysics* **1994**, *59*, 46–56. [[CrossRef](#)]
47. Perrier, F.; Morat, P. Characterization of Electrical Daily Variations Induced by Capillary Flow in the Non-saturated Zone. *Pure Appl. Geophys.* **2000**, *157*, 785–810. [[CrossRef](#)]
48. Guichet, X.; Jouniaux, L.; Pozzi, J.P. Streaming potential of a sand column in partial saturation conditions. *J. Geophys. Res. Solid Earth* **2003**, *108*. [[CrossRef](#)]
49. Darnet, M.; Marquis, G. Modelling streaming potential (SP) signals induced by water movement in the vadose zone. *J. Hydrol.* **2004**, *285*, 114–124. [[CrossRef](#)]
50. Revil, A.; Cerepi, A. Streaming potentials in two-phase flow conditions. *Geophys. Res. Lett.* **2004**, *31*. [[CrossRef](#)]
51. Revil, A.; Linde, N.; Cerepi, A.; Jougnot, D.; Matthäi, S.; Finsterle, S. Electrokinetic coupling in unsaturated porous media. *J. Colloid Interface Sci.* **2007**, *313*, 315–327. [[CrossRef](#)] [[PubMed](#)]
52. Linde, N.; Jougnot, D.; Revil, A.; Matthai, S.K.; Arora, T.; Renard, D.; Doussan, C. Streaming current generation in two-phase flow conditions. *Geophys. Res. Lett.* **2007**, *34*, L03306. [[CrossRef](#)]
53. Saunders, J.H.; Jackson, M.D.; Pain, C.C. Fluid flow monitoring in oil fields using downhole measurements of electrokinetic potential. *Geophysics* **2008**, *73*, E165–E180. [[CrossRef](#)]
54. Jackson, M.D. Multiphase electrokinetic coupling: Insights into the impact of fluid and charge distribution at the pore scale from a bundle of capillary tubes model. *J. Geophys. Res. Solid Earth* **2010**, *115*. [[CrossRef](#)]
55. Jougnot, D.; Linde, N.; Revil, A.; Doussan, C. Derivation of soil-specific streaming potential electrical parameters from hydrodynamic characteristics of partially saturated soils. *Vadose Zone J.* **2012**, *11*, 272–286. [[CrossRef](#)]

56. Revil, A.; Mahardika, H. Coupled hydromechanical and electromagnetic disturbances in unsaturated porous materials. *Water Resour. Res.* **2013**, *49*, 744–766. [[CrossRef](#)] [[PubMed](#)]
57. Allegre, V.; Jouniaux, L.; Lehmann, F.; Sailhac, P. Streaming potential dependence on water-content in Fontainebleau sand. *Geophys. J. Int.* **2010**, *182*, 1248–1266. [[CrossRef](#)]
58. Vinogradov, J.; Jackson, M.D. Multiphase streaming potential in sandstones saturated with gas/brine and oil/brine during drainage and imbibition. *Geophys. Res. Lett.* **2011**, *38*. [[CrossRef](#)]
59. Soldi, M.; Jougnot, D.; Guarracino, L. An analytical effective excess charge density model to predict the streaming potential generated by unsaturated flow. *Geophys. J. Int.* **2019**, *216*, 380–394. [[CrossRef](#)]
60. Rice, C.; Whitehead, R. Electrokinetic flow in a narrow cylindrical capillary. *J. Phys. Chem.* **1965**, *69*, 4017–4024. [[CrossRef](#)]
61. Jackson, M.D. Characterization of multiphase electrokinetic coupling using a bundle of capillary tubes model. *J. Geophys. Res. Solid Earth* **2008**, *113*. [[CrossRef](#)]
62. Linde, N. Comment on “Characterization of multiphase electrokinetic coupling using a bundle of capillary tubes model” by Mathew D. Jackson. *J. Geophys. Res. Solid Earth* **2009**, *114*, B06209. [[CrossRef](#)]
63. Guarracino, L.; Jougnot, D. A Physically Based Analytical Model to Describe Effective Excess Charge for Streaming Potential Generation in Water Saturated Porous Media. *J. Geophys. Res. Solid Earth* **2018**, *123*, 52–65. [[CrossRef](#)]
64. Thanh, L.D.; Van Do, P.; Van Nghia, N.; Ca, N.X. A fractal model for streaming potential coefficient in porous media. *Geophys. Prospect.* **2018**, *66*, 753–766. [[CrossRef](#)]
65. Thanh, L.D.; Jougnot, D.; Van Do, P.; Van Nghia, A, N. A physically based model for the electrical conductivity of water-saturated porous media. *Geophys. J. Int.* **2019**, *219*, 866–876. [[CrossRef](#)]
66. Allègre, V.; Lehmann, F.; Ackerer, P.; Jouniaux, L.; Sailhac, P. A 1-D modelling of streaming potential dependence on water content during drainage experiment in sand. *Geophys. J. Int.* **2012**, *189*, 285–295. [[CrossRef](#)]
67. Nourbehecht, B. Irreversible Thermodynamic Effects in Inhomogeneous Media and their Applications in Certain Geoelectric Problems. Ph.D. Thesis, MIT Press, Cambridge, MA, USA, 1963.
68. Morgan, F.D.; Williams, E.R.; Madden, T.R. Streaming potential properties of westerly granite with applications. *J. Geophys. Res.* **1989**, *94*, 12.449–12.461. [[CrossRef](#)]
69. Jouniaux, L.; Ishido, T. Electrokinetics in Earth Sciences: A Tutorial. *Int. J. Geophys.* **2012**, *2012*, 286107. [[CrossRef](#)]
70. Smoluchowski, M. Contribution à la théorie de l’endosmose électrique et de quelques phénomènes corrélatifs. *Bull. Int. Acad. Sci. Crac.* **1903**, *8*, 182–200.
71. Bernabé, Y. Streaming potential in heterogeneous networks. *J. Geophys. Res. Solid Earth* **1998**, *103*, 20827–20841. [[CrossRef](#)]
72. Jougnot, D.; Mendieta, A.; Leroy, P.; Mainault, A. Exploring the Effect of the Pore Size Distribution on the Streaming Potential Generation in Saturated Porous Media, Insight From Pore Network Simulations. *J. Geophys. Res. Solid Earth* **2019**, *124*, 5315–5335. [[CrossRef](#)]
73. Reppert, P.M.; Morgan, F.D.; Lesmes, D.P.; Jouniaux, L. Frequency-Dependent Streaming Potentials. *J. Colloid Interface Sci.* **2001**, *234*, 194–203. [[CrossRef](#)]
74. Li, S.X.; Pengra, D.B.; Wong, P.Z. Onsager’s reciprocal relation and the hydraulic permeability of porous media. *Phys. Rev. E* **1995**, *51*, 5748–5751. [[CrossRef](#)]
75. Pengra, D.; Li, S.X.; Wong, P. Determination of rock properties by low frequency AC electrokinetics. *J. Geophys. Res.* **1999**, *104*, 29485–29508. [[CrossRef](#)]
76. Glover, P.W.J.; Dery, N. Streaming potential coupling coefficient of quartz glass bead packs: Dependence on grain diameter, pore size, and pore throat radius. *Geophysics* **2010**, *75*, F225–F241. [[CrossRef](#)]
77. Ishido, T.; Mizutani, H. Experimental and Theoretical Basis of Electrokinetic Phenomena in Rock-Water Systems and Its Applications to Geophysics. *J. Geophys. Res.* **1981**, *86*, 1763–1775. [[CrossRef](#)]
78. Jouniaux, L.; Pozzi, J.P. Laboratory measurements anomalous 0.1–0.5 Hz streaming potential under geochemical changes: Implications for electrotelluric precursors to earthquakes. *J. Geophys. Res. Solid Earth* **1997**, *102*, 15335–15343. [[CrossRef](#)]
79. Jaafar, M.Z.; Vinogradov, J.; Jackson, M.D. Measurement of streaming potential coupling coefficient in sandstones saturated with high salinity NaCl brine. *Geophys. Res. Lett.* **2009**, *36*. [[CrossRef](#)]

80. Johnson, D.L.; Koplik, J.; Schwartz, L.M. New Pore-Size Parameter Characterizing Transport in Porous Media. *Phys. Rev. Lett.* **1986**, *57*, 2564–2567. [[CrossRef](#)] [[PubMed](#)]
81. Kormiltsev, V.V.; Ratushnyak, A.N.; Shapiro, V.A. Three-dimensional modeling of electric and magnetic fields induced by the fluid flow movement in porous media. *Phys. Earth Planet. Inter.* **1998**, *105*, 109–118. [[CrossRef](#)]
82. Revil, A.; Leroy, P. Constitutive equations for ionic transport in porous shales. *J. Geophys. Res. Solid Earth* **2004**, *109*, B03208. [[CrossRef](#)]
83. Cerepi, A.; Cherubini, A.; Garcia, B.; Deschamps, H.; Revil, A. Streaming potential coupling coefficient in unsaturated carbonate rocks. *Geophys. J. Int.* **2017**, *210*, 291–302. [[CrossRef](#)]
84. Jougnot, D.; Roubinet, D.; Guarracino, L.; Maineult, A. *Modeling Streaming Potential in Porous and Fractured Media, Description and Benefits of the Effective Excess Charge Density Approach*; Biswas, A., Sharma, S., Eds.; Advances in Modeling and Interpretation in Near Surface Geophysics; Springer Geophysics; Springer: Cham, Switzerland, 2020.
85. Bassiouni, Z. *Theory, Measurement, and Interpretation of Well Logs*; Henry L. Doherty Memorial Fund of AIME, Society of Petroleum Engineers: Dallas, TX, USA, 1994.
86. Mandelbrot, B.B. *The Fractal Geometry of Nature*; W. H. Freeman: New York, NY, USA, 1982.
87. Katz, A.J.; Thompson, A.H. Fractal Sandstone Pores: Implications for Conductivity and Pore Formation. *Phys. Rev. Lett.* **1985**, *54*, 1325–1328. [[CrossRef](#)]
88. Yu, B.; Cheng, P. A fractal permeability model for bi-dispersed porous media. *Int. J. Heat Mass Transf.* **2002**, *45*, 2983–2993. [[CrossRef](#)]
89. Yu, B. Analysis of Flow in Fractal Porous Media. *Appl. Mech. Rev.* **2008**, *61*, 050801. [[CrossRef](#)]
90. Jurin, J., II. An account of some experiments shown before the Royal Society; with an enquiry into the cause of the ascent and suspension of water in capillary tubes. *Philos. Trans. R. Soc. Lond.* **1719**, *30*, 739–747.
91. Waxman, M.H.; Smits, L.J.M. Electrical conductivities in oil bearing shaly sands. *Soc. Pet. Eng. J.* **1968**, *8*, 107–122. [[CrossRef](#)]
92. Thanh, L.D. Effective Excess Charge Density in Water Saturated Porous Media. *VNU J. Sci. Math. Phys.* **2018**, *34*. [[CrossRef](#)]
93. Revil, A.; Cathles, L.M., III; Manhardt, P.D. Permeability of shaly sands. *Water Resour. Res.* **1999**, *3*, 651–662. [[CrossRef](#)]
94. Glover, P.W.; Zadjali, I.I.; Frew, K.A. Permeability prediction from MICP and NMR data using an electrokinetic approach. *Geophysics* **2006**, *71*, F49–F60. [[CrossRef](#)]
95. Sen, P.; Scala, C.; Cohen, M.H. A self-similar model for sedimentary rocks with application to the dielectric constant of fused glass beads. *J. Soil Mech. Found. Div.* **1981**, *46*, 781–795. [[CrossRef](#)]
96. Glover, P.W.J.; Walker, E. Grain-size to effective pore-size transformation derived from electrokinetic theory. *Geophysics* **2009**, *74*, E17–E29. [[CrossRef](#)]
97. Revil, A.; Glover, P.W.J. Nature of surface electrical conductivity in natural sands, sandstones, and clays. *Geophys. Res. Lett.* **1998**, *25*, 691–694. [[CrossRef](#)]
98. Wildenschild, D.; Roberts, J.J.; Carlberg, E.D. On the relationship between microstructure and electrical and hydraulic properties of sand-clay mixtures. *Geophys. Res. Lett.* **2000**, *27*, 3085–3088. [[CrossRef](#)]
99. Bolève, A.; Crespy, A.; Revil, A.; Janod, F.; Mattiuzzo, J.L. Streaming potentials of granular media: Influence of the Dukhin and Reynolds numbers. *J. Geophys. Res.* **2007**, *112*. [[CrossRef](#)]
100. Cai, J.C.; Hu, X.Y.; Standnes, D.C.; You, L.J. An analytical model for spontaneous imbibition in fractal porous media including gravity. *Colloids Surf. A Physicochemical Eng. Asp.* **2012**, *414*, 228–233. [[CrossRef](#)]
101. Sen, P.N.; Goode, P.A. Influence of temperature on electrical conductivity on shaly sands. *Geophysics* **1992**, *57*, 89–96. [[CrossRef](#)]
102. Dullien, F.A.L. *Porous Media: Fluid Transport and Pore Structure*; Academic: San Diego, CA, USA, 1992.
103. Bull, H.B.; Gortner, R.A. Electrokinetic potentials. X. The effect of particle size on the potential. *J. Phys. Chem.* **1932**, *36*, 111–119. [[CrossRef](#)]

104. Cherubini, A.; Garcia, B.; Cerepi, A.; Revil, A. Streaming Potential Coupling Coefficient and Transport Properties of Unsaturated Carbonate Rocks. *Vadose Zone J.* **2018**, *17*, 180030. [[CrossRef](#)]
105. Archie, G.E. The electrical resistivity log as an aid in determining some reservoir characteristics. *Pet. Trans. AIME* **1942**, *146*, 54–62. [[CrossRef](#)]



© 2020 by the authors. Licensee MDPI, Basel, Switzerland. This article is an open access article distributed under the terms and conditions of the Creative Commons Attribution (CC BY) license (<http://creativecommons.org/licenses/by/4.0/>).